Journal of Power Sources 360 (2017) 301–318

Contents lists available at ScienceDirect

Journal of Power Sources

journal homepage: www.elsevier.com/locate/jpowsour

A Comparison between Electrochemical Impedance Spectroscopy and Incremental Capacity-Differential Voltage as Li-ion Diagnostic Techniques to Identify and Quantify the Effects of Degradation Modes within Battery Management Systems

Carlos Pastor-Fernández [a, *], Kotub Uddin [a], Gael H. Chouchelamane [b], W. Dhammika Widanage [a], James Marco [a]

[a] WMG, University of Warwick, Coventry, CV4 7AL, UK
[b] Jaguar Land Rover, Banbury Road, Warwick, CV35 0XJ, UK

HIGHLIGHTS

- Degradation modes (DMs) evaluated within parallel connected cells.
- A novel method to quantify the effect of DMs using EIS and IC-DV is presented.
- LLI, LAM are the most pertinent DMs obtained with each technique.
- The effect of the DMs obtained with EIS and IC-DV are correlated.
- On-board implementation of EIS and IC-DV within a BMS is discussed.

GRAPHICAL ABSTRACT

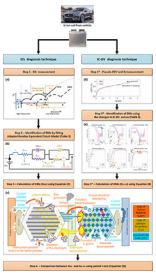

ARTICLE INFO

Article history:
Received 21 December 2016
Received in revised form
16 February 2017
Accepted 11 March 2017

Keywords:
Lithium ion technology
Battery management system
Electrochemical impedance spectroscopy
Incremental capacity analysis
Differential voltage analysis
Degradation modes

ABSTRACT

Degradation of Lithium-ion batteries is a complex process that is caused by a variety of mechanisms. For simplicity, ageing mechanisms are often grouped into three degradation modes (DMs): conductivity loss (CL), loss of active material (LAM) and loss of lithium inventory (LLI). State of Health (SoH) is typically the parameter used by the Battery Management System (BMS) to quantify battery degradation based on the decrease in capacity and the increase in resistance. However, the definition of SoH within a BMS does not currently include an indication of the underlying DMs causing the degradation. Previous studies have analysed the effects of the DMs using incremental capacity and differential voltage (IC-DV) and electrochemical impedance spectroscopy (EIS). The aim of this study is to compare IC-DV and EIS on the same data set to evaluate if both techniques provide similar insights into the causes of battery degradation. For an experimental case of parallelized cells aged differently, the effects due to LAM and LLI were found to be the most pertinent, outlining that both techniques are correlated. This approach can be further implemented within a BMS to quantify the causes of battery ageing which would support battery lifetime control strategies and future battery designs.

1. Introduction

In the recent years, battery electric and plug hybrid electric vehicles (BEV and PHEV) have been presented as an alternative

* Corresponding author.
E-mail address: c.pastor-fernandez@warwick.ac.uk (C. Pastor-Fernández).

http://dx.doi.org/10.1016/j.jpowsour.2017.03.042
0378-7753/

road transport mode to conventional internal combustion engine (ICE) based vehicles due to their high energy efficiency and low tail pipe emissions. Vehicle battery systems are typically equipped with a high number of cells connected electrically in parallel and series to meet the requirements of energy and power. During battery life, the available energy and power that may be extracted from the battery is known to reduce due to degradation. Degradation of lithium-ion batteries (LIBs) is an extremely complex process that depends on a variety of ageing mechanisms caused by different intrinsic and extrinsic factors [1,2]. Intrinsic factors include inconsistencies in manufacturing processes and in the materials used. Intrinsic factors are currently mitigated by improving quality control, manufacturing processes and battery designs. Extrinsic factors include those due to the inhomogeneous operating conditions that a LIB may be subject to, e.g. non-uniform current or temperature distribution within the complete battery pack. In order to reduce battery degradation, the Battery Management System (BMS) mitigates the impact of extrinsic factors by setting a number of variables that include, but are not constrained to: the level of charge or discharge power, the temperature range that the battery operates over and the allowable depth of discharge (DoD) of the battery. State of Health (SoH) is typically the parameter used by the BMS to quantify battery degradation with respect to its nominal state and it is often quantified based on two measures: capacity fade (CF) and power fade (PF) [3]. These metrics are directly related to available driving range and power, respectively. However, the definition of SoH within a BMS does not currently include an indication of the underpinning ageing mechanisms causing the degradation.

There are many different ageing mechanisms and to aid in their understanding and interpretation, they are commonly grouped into three different degradation modes (DMs): conductivity loss (CL), loss of active material (LAM) and loss of lithium inventory (LLI) [4]. CL includes the degradation of the electronic parts of the battery such as current collector corrosion or binder decomposition [5]. LAM is related to structural transformations in the active material and electrolyte decomposition [5]. LLI is attributed to the variation of the number of lithium-ions (Li-ions) that are available for intercalation and de-intercalation processes [5].

Several techniques are commonly applied and reported within the literature to identify and quantify the effects of DMs. These are often classified into in-situ and ex-situ electrochemical techniques. In-situ electrochemical methods are not-invasive characterisation techniques, potentially making them suitable for real-time applications within a BMS. Examples of in-situ methods are Incremental Capacity (IC) and Differential Voltage (DV) [2,4,6], Electrochemical Impedance Spectroscopy (EIS) [7,8,9] and Differential Thermal Voltammetry (DTV) [10,11].

Ex-situ methods consist of applying physicochemical and electrochemical invasive techniques to study the cells internally. Scanning Electron Microscopy (SEM), Energy Dispersive Spectrometry (EDS) or X-Ray Diffractometry (XRD) [12] are commonly used examples. It is beyond the scope of this paper to discuss each of these techniques; they are however described fully in a number of references [12].

In-situ health diagnosis techniques were shown to be effective tools to analyse DMs of single Li-ion cells. In automotive applications, however, the majority of battery pack configurations connect cells in parallel first to form small modules, and then align the modules in series to form the pack [13]. The main difference between a single cell and a module that has cells connected in parallel is the existence of uneven current distribution when cell properties change due to manufacturing tolerances or usage conditions [3]. For instance, the presence of temperature gradients or different resistance paths within an automotive battery pack will lead to uneven current distribution in the short-term and to cell-to-cell SoH differences in the long-term [14]. Another application of this study is second life grid energy storage applications in which battery modules (of different SoH) may be connected together either in series or parallel to form the complete battery assembly [3]. Understanding the reasons for battery ageing under real operating conditions is needed to improve lifetime control strategies within BMSs and the design of new batteries and manufacturing processes, so that the impact of intrinsic and extrinsic factors on battery ageing can be better mitigated.

From a review of the published literature the authors have identified that two suitable techniques to identify and quantify the effects of DMs are EIS [8,15] and IC-DV [2,4] because they can infer the effects of the different DMs in a mechanistic way and thus, they can be implemented on-board in future BMS real-time applications [16–19]. In line with this, the contribution of this work is twofold. Firstly, a step-by-step methodology to identify and quantify the effects of the DMs is proposed as illustrates in Fig. 1. EIS and IC-DV techniques based on full cell measurements were used to identify and quantify the DMs. Secondly, the results obtained from each technique are critically evaluated and compared within the context of their on-board implementation within a BMS application. To make the analysis of these techniques close to a real application, this study considers the data set from four cells connected in parallel emulating an imbalanced battery module scenario. Each cell's initial SoH was different, which is a typical scenario when battery ageing may ultimately cause a failure in a module due to uneven current distribution through each cell connected in parallel.

The structure of this work is divided as follows: Section 2 explains the most common DMs and ageing mechanisms in LIBs, focusing on the Nickel Cobalt Aluminum - Carbon (NCA-C) cell type. Section 3 gives a background of the EIS and IC-DV diagnosis techniques, describing the methodology employed to identify and quantify the effects of DMs. Section 4 summarises the experimental investigation conducted for this work and Section 5 presents the results. Using the approach described in Section 3, Section 6 identifies and quantifies the DMs, and their relationship to SoC and initial degradation of each cell connected in parallel. Furthermore, the results obtained with EIS and IC-DV are compared and their applicability for embedded use with a BMS are discussed. Section 7 describes the limitations of this work, outlining areas that need to be further investigated and finally, Section 8 presents the main conclusions of this study.

2. Degradation modes and ageing mechanisms in lithium-ion batteries

NCA-C cells are a candidate solution for BEV and PHEV applications due to their high operating voltage window (2.5–4.2 V), high specific discharge capacity (155 mAh g^{-1}) and high specific energy (200–260 Wh kg^{-1}) [20]. The most relevant drawbacks are reliability problems at high temperatures (>40 °C) and relatively high cost of the bulk cobalt (circa: 0.03 £ g^{-1} - 2016) [21] that forms the cell cathode.

From an electrochemical viewpoint, the general causes that lead to CL, LLI or LAM can be very diverse as illustrated in Fig. 1 (c). LLI ageing mechanisms are electrolyte decomposition, lithium plating and formation of Li-ion grains [1]. CL ageing mechanisms are current collector corrosion and binder decomposition [1]. LAM ageing mechanisms are oxidation of the electrolyte, electrode decomposition, intercalation gradient strains in the active particles, and crystal structure disorder [1].

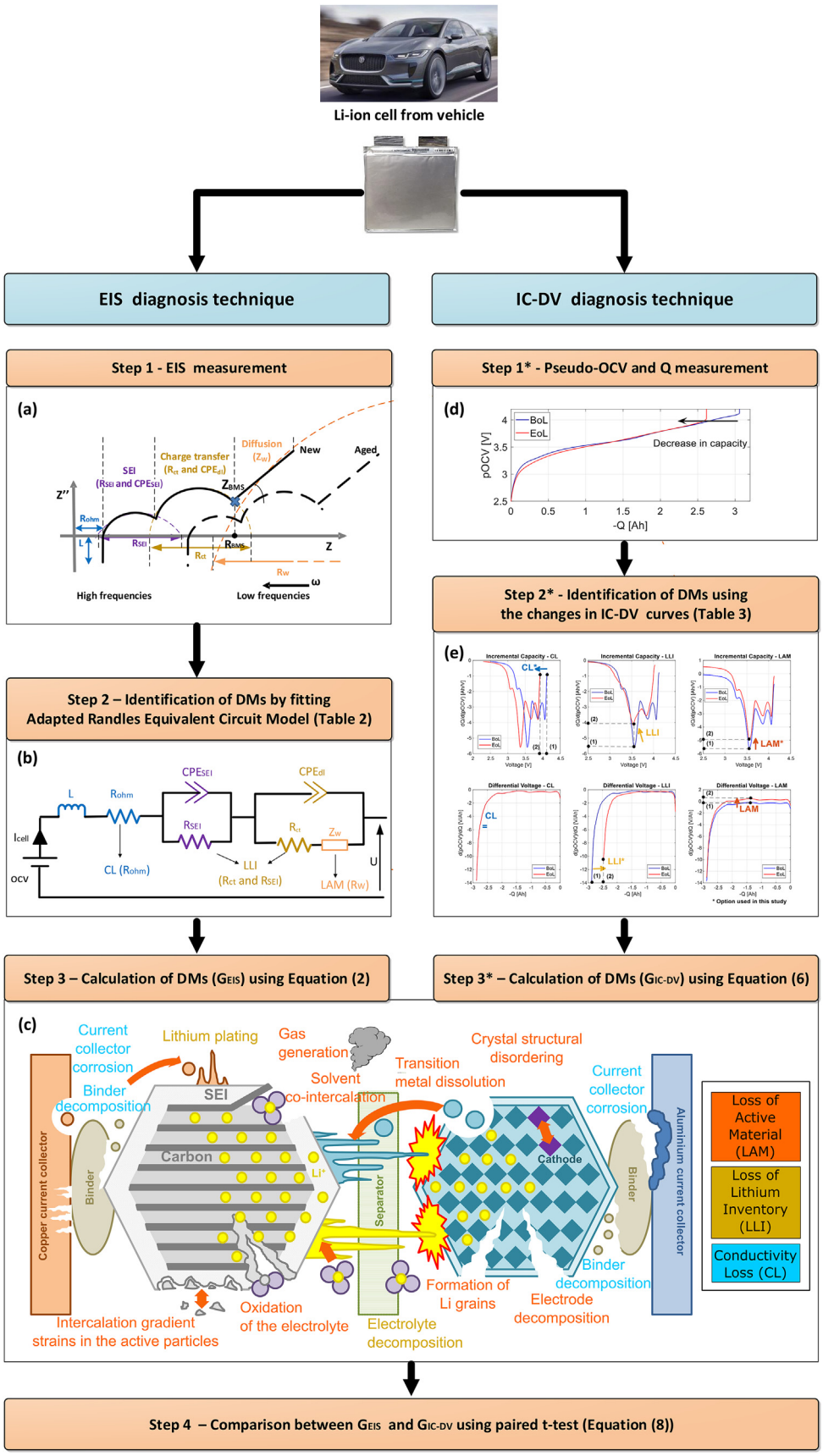

Fig. 1. Framework of the methodology employed within this study. (a) Relationship of EIS spectrum with kinetic Li-ion battery processes; (b) relationship of Adapted Randles-Equivalent Circuit Model (AR-ECM) components with DMs; (c) DMs and ageing mechanisms in LIBs, adapted from [1,2,22]; (d) pseudo-OCV curve, (e) relationship of changes in IC and DV curves with the DMs.

Uddin et al. [1] suggested a generic relationship between battery ageing extrinsic factors (temperature, C-rate, SoC, ΔDoD and cycle number) and the affected component (positive or negative electrode) with the corresponding ageing mechanism and potential effects for LIBs. Table 1 extends this relationship suggesting the most pertinent observed effects (CF or/and PF) and DM (CL, LLI or LAM) for each potential ageing effect. Previous studies that have examined the ageing mechanisms within LIBs [5,23] were also considered to establish this relationship. For the particular case of the NCA-C technology, previous work [24–29] studied the most significant ageing mechanisms under storage and cycling conditions. The authors concluded that degradation is mainly accelerated under cycling conditions onto the cathode side [25,26], due to micro-cracking generation (LAM) and growth of NiO-like structure layer (LLI) [28,29]. These DMs are exacerbated at large DoD (e.g. greater than 80%) and high temperature (above 60 °C) [27–29]. Based on Table 1 and comparable studies from the literature [24–29], it was hypothesized that for the experiment of this study the cells would age due to a large ΔDoD (100%) and high cycle number (500 cycles). The other conditions at which the cells were tested in this study are between the levels in which accelerated ageing is not expected according to Table 1 (C/2 for charge and 1 C for discharge, temperature 25 °C ± 1 °C and continuous SoC from 0% to 100%). The experimental conditions of this study are described further in detail in Section 4.

Table 1
Relationship of the battery ageing extrinsic factors with the affected component, ageing mechanism, potential ageing effects, most pertinent observed effects and most pertinent DM. Extended from Refs. [1,5].

Extrinsic factor	Level	Affected component	Ageing mechanism	Potential ageing effects	Most pertinent observed effects	Most pertinent DM
T	High (>35 °C)	NE	Electrolyte decomposition.	SEI growth.	PF	LLI
				Micro pore clogging.	CF & PF	LLI
				SEI dissolution.	CF & PF	LAM
			Transition metal dissolution.	Precipitation of new phases.	PF	LAM
				Formation of dendrites.	PF	LAM
		PE	Oxidation of electrolyte.	SPI growth.	PF	LLI
				Gas generation.	CF	LAM
			Electrode decomposition.	Precipitation of new phases.	CF & PF	LAM
T	Low (<5 °C)	NE	Lithium plating.	Dendrite growth.	CF & PF	LLI
				SEI formation.	CF & PF	LLI
			Intercalation gradient strains in the active particles (with cycling).	Interstitial site loss.	CF & PF	LAM
C-rate	High (>2C)	NE	Lithium plating.	SEI formation.	CF & PF	LLI
			Intercalation gradient strains in the active particles (with cycling).	Interstitial site loss.	CF	LAM
			Formation of Li grains.	Graphite exfoliation.	CF	LAM
				Isolation of active material.	CF	LAM
				SEI formation and growth.	PF	LLI
SoC	Low (<0%)	NE (high potential)	Current collector corrosion.	Loss of conductivity.	PF	CL
		PE (low potential)	Crystal structure disordering.	Phase change.	CF & PF	LAM
			Binder decomposition.	Loss of conductivity.	PF	CL
SoC	High (>95%)	NE (low potential)	Binder decomposition.	Loss of conductivity.	CF	CL
			Transition metal dissolution.	Precipitation of new phases.	PF	LAM
				Formation of dendrites.	PF	LAM
			Solvent co-intercalation.	Phase change.	CF & PF	LAM
				SEI growth.	CF & PF	LLI
		PE (high potential)	Electrode decomposition.	Precipitation of new phases.	PF	LAM
				Exfoliation of active material.	CF	LAM
				Gas generation.	CF	LAM
			Transition metal dissolution.	Phase change.	CF & PF	LAM
ΔDoD	Large (>70%)	PE & NE	Intercalation gradient strains in the active particles.	Volume change.	CF	LAM
			Crystal structural disordering.	Particle cracking.	PF	LAM
			Solvent co-intercalation.	Phase change.	CF & PF	LAM
				SEI growth.	CF & PF	LLI
Cycle number	High[a]	NE & PE	Intercalation gradient strains in the active particles.	Volume change.	CF	LAM
			Crystal structure disordering.	Phase change.	CF & PF	LAM
				Particle cracking.	PF	LAM

[a] Equivalent to 2/3 of capacity decrease or resistance increase with respect to their Beginning of Life values.

Table 2
Relationship between the resistances of the AR-ECM with the most pertinent DM, potential ageing mechanisms and most pertinent observed effects.

AR-ECM component	Unit	Most pertinent DM	Potential ageing mechanisms	Most pertinent observed effects
Increase in R_{ohm}	[Ω]	CL	Current collector corrosion.	PF
			Binder decomposition.	CF
Increase in R_{SEI} & R_{ct}	[Ω]	LLI	Electrolyte decomposition.	CF & PF
			Oxidation of electrolyte.	PF
			Lithium plating.	CF & PF
			Formation of Li grains.	CF & PF
			Solvent co-intercalation.	CF & PF
Increase in R_W	[Ω]	LAM	Electrode decomposition.	CF & PF
			Oxidation of the electrolyte.	CF & PF
			Intercalation gradient strains in the active particles.	CF & PF
			Formation of Li grains.	CF
			Crystal structure disordering.	CF & PF
			Transition metal dissolution.	PF
			Solvent co-intercalation.	CF & PF

3. Non-destructive battery health diagnosis techniques

3.1. Electrochemical impedance spectroscopy (EIS)

EIS is a widely used experimental technique to gain a deeper insight into the electrochemical processes of LIBs. EIS results are usually represented by a Nyquist plot, where the imaginary and the real part of the impedance are plotted on the ordinate (y-axis) and abscissa (x-axis), respectively. The internal impedance is often defined as the low frequency turning point of the EIS plot [3]. Fitting the Nyquist plot (Fig. 1 (a)) to a LIB Equivalent Circuit Model (ECM) (Fig. 1 (b)) allows the battery kinetic processes (Solid Electrolyte Interphase (SEI), charge-transfer and diffusion) to be modeled.

The Adapted Randles ECM (AR-ECM), which is a commonly used ECM in the literature [6,7], is employed in this study. Fig. 1 (b) illustrates that the AR-ECM is composed of a voltage source connected in series with a resistor; an inductor and resistor; and, Constant Phase Elements (CPEs) parallel branches. CPEs are employed to represent the porosity and tortuosity characteristics of the electrodes [30]. However, they are often simplified to capacitors to facilitate easier numerical simulation within the time-domain. This simplification is known to reduce the accuracy of the model [31].

3.2. Identification of degradation modes using EIS

This work proposes to track the change of the AR-ECM resistances (ohmic, SEI, charge-transfer and Warburg) to identify and quantify the effects of DMs as suggested in Ref. [9].

The elements of the AR-ECM are derived by fitting the EIS spectrum. According to Fig. 1 (a), R_{ohm} is quantified as the horizontal distance between the zero and the point where the EIS spectrum crosses the real axis (high frequencies); and R_{SEI}, R_{ct} and R_{W} are calculated as the horizontal distances of the each depressed semicircle, respectively. It is noteworthy to mention that the diffusion semicircle is not shown completely due to the limitations in the size of the figure.

Tracking the resistance is beneficial as the resistance increase is an indicator of power fade which is used to define $\mathrm{SoH_P}$ and, secondly, the AR-ECM resistances are related to the dynamic behaviour of the battery, which, can be further linked to key DMs [7]. It is known that one AR-ECM resistance comprises the change of more than a single DM, and theoretically it is not possible to isolate the causality between a single ageing mechanism, DM and electrical component within an ECM representation. Table 2 proposes a relationship between each resistance of the AR-ECM and the most significant effects of the DMs and ageing mechanisms. This relationship is a first step to link each resistance of the AR-ECM with individual effects of DMs. For instance, other studies such as Ref. [32] proposed an alternative procedure to relate AR-ECM resistances with the effects of DMs. Therefore, there is no an unique method to relate AR-ECM resistances with the effects of DMs, and thus, further work is required in this respect.

R_{ohm} is used to model the resistance in the current collectors, connectors and electrolyte [33]. Corrosion of current collectors and connectors as well as changes in the electrolyte composites due to side reactions cause CL through ageing. CL is manifested as voltage drops through the R_{ohm}. Thus, the increase of R_{ohm} can be used as a measure of the increase in CL.

SEI (formation, build-up and decomposition) is one of the most relevant ageing mechanisms in Li-ion batteries. SEI impedes the intercalation and de-intercalation of Li-ions between the electrolyte and the anode. This interphase leads in turn to the irreversible consumption of Li-ions (LLI), which results in pronounced capacity fade and increased resistance [5]. Hence, the increase of R_{SEI} is a consequence of LLI. Apart from the SEI, there are other degradation effects such as dendrite growth or micro pore clogging (refer to Table 1) that are mainly attributable to LLI. From the perspective of the dynamics of the cell's voltage response, these effects as well as SEI are translated into a reduction of the charge-transfer Li-ion intercalation and de-intercalation reactions [5], which is seen as an increase of the R_{ct}. Thus, the increase of R_{ct} is also a consequence of LLI. This points out that LLI is related to more than one resistance, R_{SEI} and R_{ct}.

Diffusion is caused when the concentration level within a Li-ion particle is different. This leads to structural transformations in the Li-ion particle and between different Li-ion particles [5,26,34]. Diffusion processes are modeled by a Warburg impedance, Z_W. The Warburg impedance is calculated as a function of the current I, the frequency ω, the specific diffusion thickness l, the effective diffusion coefficient of the particle D and the phase angle coefficient between the current and the applied voltage n [31] as shown Equation (1).

$$Z_W = R_W \cdot \frac{\tanh\left(\left(I\frac{l^2}{D}\omega\right)^{\mathrm{n}}\right)}{I\frac{l^2}{D}\omega} \tag{1}$$

R_W depends on the effective diffusion path length (L^2/D term), and since diffusion processes are related to morphological changes in the structure of the electrodes then the increase of R_W can be attributed mostly to LAM.

3.2.1. Quantification of degradation modes using EIS

The growth in percentage, G_{EIS}, is the parameter proposed to quantify the effects of DMs over cycle number. G_{EIS} is a set of metrics calculated for each characterisation test k, cell i and SoC q using Equation (2). The number and type of the characterisation test performed in this experiment are described further in Section 4.

$$G_{EIS} = \begin{cases} \mathrm{CL}^{q}_{EIS,k,i}(\%) = \dfrac{\left(R^{q}_{ohm,k,i} - R^{q}_{ohm,1,i}\right)}{R^{q}_{ohm,1,i}} \cdot 100 \\ \mathrm{LLI}^{q}_{EIS,k,i}(\%) = \dfrac{\left(R^{q}_{SEI,k,i} - R^{q}_{SEI,1,i}\right) + \left(R^{q}_{ct,k,i} - R^{q}_{ct,1,i}\right)}{R^{q}_{SEI,1,i} + R^{q}_{ct,1,i}} \cdot 100 \\ \mathrm{LAM}^{q}_{EIS,k,i}(\%) = \dfrac{\left(R^{q}_{W,k,i} - R^{q}_{W,1,i}\right)}{R^{q}_{W,1,i}} \cdot 100 \end{cases} \quad (2)$$

For $k = 1 \ldots 11$, $q = 20\%, 50\%, 90\%$ and $i = 1 \ldots 4$.

These equations are used in Section 6.1 to quantify the effects of DMs based on the EIS technique.

3.3. Incremental capacity (IC) and differential voltage (DV)

IC-DV analysis is a method used to identify and quantify changes in the electrochemical properties of the cell based on differences in the charge Q, and pseudo-OCV (pOCV) when the cell is assumed to be at equilibrium. An approximate equilibrium state is achieved if the cell is typically charged or discharged at very low currents (circa: ≤C/25) whilst measuring the Q and the pOCV [4]. However, charging and discharging the cell at such low currents is difficult to perform in a real application since the time required would be prohibitive [19]. A current of C/10 was therefore employed to generate the required pOCV curves as suggested in Ref. [35]. This represents a compromise between a true state of equilibrium measurement and a pragmatic solution that may be feasibly employed within a BMS. The IC and DV curves (Fig. 1 (e)) are obtained from differentiating Q and pOCV measurements (Fig. 1 (d)). Despite the fact that IC and DV curves are determined from the Q and pOCV relationship, both curves offer different insights into the rate and nature of the degradation within the cell. Mathematically, the IC curve was computed as the gradient of Q with respect to *pOCV* using Equation (3). The *gradient* function in MATLAB© is employed to perform this calculation.

$$\frac{dQ}{d(pOCV)} \approx \frac{\Delta Q}{\Delta(pOCV)} \quad (3)$$

Calculating the inverse of the IC curve yields the DV curve. Mathematically, the DV curve is derived as the gradient of *pOCV* with respect to *Q* using Equation (4).

$$\frac{d(pOCV)}{dQ} \approx \frac{\Delta(pOCV)}{\Delta Q} \quad (4)$$

The measurements of the charge and the pOCV are often disturbed by noise. To filter the amount of noise in the measurements the IC and DV curves are smoothed before the derivatives are computed. The filtering procedure firstly consists of averaging *pOCV* values which are related to any repeated charge measurements, and secondly linear interpolating the remaining data points so that *pOCV* values exist at equally spaced *Q* values. The smoothed data was compared to the original data set to evaluated whether the smoothed data still accurately followed the original data. This was done by ensuring that the median of the absolute deviations of the recorded dataset about the smoothed line is below 2%. As it is showed in Section 6, this difference enables us to infer the DMs clearly and therefore it is suitable for the object of this study.

For automotive applications deriving the pOCV curve during

Table 3
Relationship between the changes in IC-DV curves with the most pertinent DM, potential ageing mechanisms and most pertinent observed effects.

Change in IC curve	Unit	Change in DV curve	Unit	Most pertinent DM	Potential ageing mechanisms	Most pertinent observed effects
Shifting toward lower voltages.	[V]	Lack of change.	[Ah]	CL	Current collector corrosion.	PF
					Binder decomposition.	CF
Decrease of the height of the peaks and shift toward lower or higher voltages.	[Ah V^{-1}] and [V]	Shifting toward lower capacities.	[Ah]	LLI	Electrolyte decomposition.	CF & PF
					Oxidation of electrolyte	PF
					Lithium plating.	CF & PF
					Formation of Li grains.	CF & PF
					Solvent co-intercalation.	CF & PF
Decrease of the height of the peaks at approximately constant voltage.	[Ah V^{-1}]	Decrease of the depth of valleys at approximately constant capacity.	[V Ah^{-1}]	LAM	Electrode decomposition.	CF & PF
					Oxidation of the electrolyte.	CF & PF
					Intercalation gradient strains in the active particles.	CF & PF
					Formation of Li grains.	CF
					Crystal structure disordering.	CF & PF
					Transition metal dissolution.	PF
					Solvent co-intercalation.	CF & PF

Table 4
Experimental test matrix (adapted from Ref. [3]).

Cell	Test	# ageing cycles (individual cells) [#cycles]	# test cycles (cells connected in parallel) [#cycles]	# cycles (individual + parallel cells) [#cycles]	Testing procedure	T [°C]	ΔDoD [%]	t_{samp} [s]
1	Cycling	0	500	500	CC-CV chg and 1C dchg	25	100	1
	Characterisation	Every 50 cycles	Every 50 cycles	–	1C dchg, EIS test and pOCV	25	100	1
2	Cycling	50	500	550	CC-CV chg and 1C dchg	25	100	1
	Characterisation	Every 50 cycles	Every 50 cycles	–	1C dchg, EIS test and pOCV	25	100	1
3	Cycling	100	500	600	CC-CV chg and 1C dchg	25	100	1
	Characterisation	Every 50 cycles	Every 50 cycles	–	1C dchg, EIS test and pOCV	25	100	1
4	Cycling	150	500	650	CC-CV chg and 1C dchg	25	100	1
	Characterisation	Every 50 cycles	Every 50 cycles	–	1C dchg, EIS test and pOCV	25	100	1

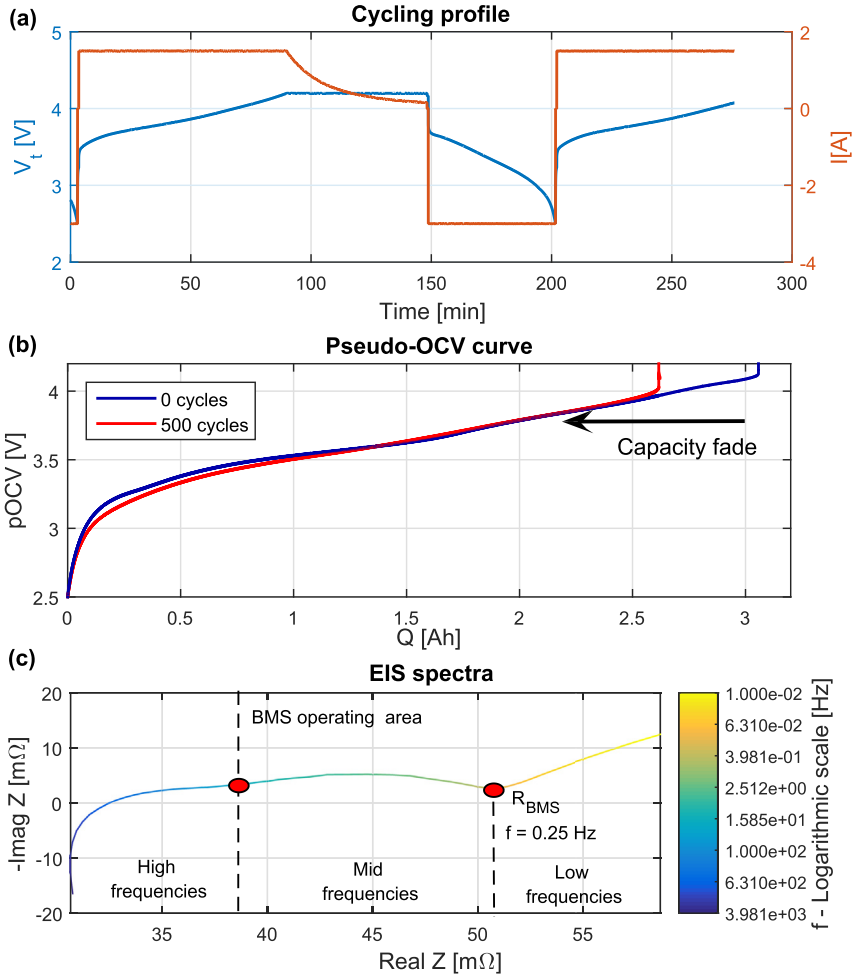

Fig. 2. (a) Charge-discharge cycling profile employed to age the cells connected in parallel, (b) pOCV-SoC curve of cell 1 for 0 and 500 cycles for a discharge event, (c) EIS spectrum of cell 1 for 0 cycle at SoC 50% with respect to the frequency showing BMS operating area and R_{BMS} [3].

operation is easier during charging than during discharging since the discharging process cannot be controlled as it depends on the driving conditions. However, if the pOCV measurements are obtained under laboratory conditions, the difficulty of obtaining the pOCV curve is the same for both charging and discharging. In addition, the DMs can be different between charge and discharge since pOCV measurements have a maximum difference of 20 mV for the case of a Nickel Cobalt Manganese (NCM) 2.2 Ah cell as shown in Ref. [36]. For this work only the discharge was used to generate the pOCV measurements. However, further work includes the evaluation of the DMs using pOCV measurements during charging to quantify the differences with respect to the DMs derived from discharging.

3.4. Identification of degradation modes using IC-DV

This work uses the conclusions derived from Dubarry et al. [4] to identify the DMs by means of full cell IC and DV curves.

Consistent with Table 2 (EIS case), Table 3 relates the change in the IC-DV curves with the most pertinent DM as suggested in

Dubarry et al. [4]. Shifting toward lower voltages (IC) and constant capacity (DV) are related to CL; decrease of the height of the peaks and shift toward lower or higher voltages (IC) and shifting toward lower capacities (DV) are linked to LLI; and, decrease of the height of the peaks at approximately constant voltage (IC) and decrease of the depth of the valleys at approximately constant capacity (DV) are correlated to LAM.

Assuming a simple ECM representation of the battery to Ohm's law, the pOCV voltage, V_{poc}, is derived as the difference between the pure OCV, V_{oc}, and the voltage drop due to the ohmic resistance, V_{ohm}, as shown in Equation (5).

$$V_{poc} = V_{oc} - V_{ohm} = V_{oc} - I \cdot R_{ohm} \tag{5}$$

Given a constant current flow and V_{oc}, an increase in R_{ohm} will cause a decrease in V_{poc}. As described in Section 3.2, the increase in R_{ohm} is related to CL [33]. This means that the increase in R_{ohm} only affects the cell voltage, not the capacity [4]. Therefore, without capacity fade, the effect of CL can be seen as a shift of the IC curve to lower voltages and as a lack of change in the DV curves [4].

A reduction in the number of charge-transfer Li-ion intercalation and de-intercalation reactions leads to a decrease of the V_{oc} and the charge (capacity). These effects are mainly linked to LLI as described in Section 3.2. Visually, this is translated into a decrease of the height of the peaks and shift toward lower or higher voltages (IC), and a shift toward lower capacities (DV).

A decrease of the magnitude of the peaks in the IC curve represents a reduction of the charge at an approximately constant V_{poc}. Similarly, reduction of the depth of the valleys in the DV curve represents a reduction of the V_{poc} phase change at an approximately constant charge. For both cases, the V_{poc} or charge changes slightly, and so implies the system is close to equilibrium and therefore the total overpotential is approximately zero. From an electrochemical viewpoint this scenario involves the movement of a low amount of Li-ions and therefore, these phase changes are mostly attributed to structure disordering of the active materials (LAM) [4,12].

3.5. Quantification of degradation modes using IC-DV

As for the EIS case, the growth in percentage, G_{IC-DV}, is the metric derived to quantify the effects of DMs. The G_{IC-DV} is quantified based on the changes of the IC and DV curves (for the case of two characterisation tests, refer to points (1) and (2) in Fig. 1 (e)). The points (1) and (2) are the maximum value of the pOCV, *max(pOCV)*, to determine the G_{IC-DV} due to CL; the absolute of the maximum value of the charge, *max(Q)*, to calculate the G_{IC-DV} due to LLI; and the absolute of the maximum value of the phase change in charge with respect to the phase change in pOCV, $max\left(\frac{\Delta Q}{\Delta pOCV}\right)$, to quantify the G_{IC-DV} due to LAM. Considering the absolute values of the $max(Q)$ and the $max\left(\frac{\Delta Q}{\Delta pOCV}\right)$ enables the use of G_{IC-DV} independently for charge or discharge pOCV measurements. The G_{IC-DV} is computed for each characterisation test k and cell i using Equation (6).

$$G_{iC-DV} = \begin{cases} \mathrm{CL}_{IC-DV,k,i}(\%) = \dfrac{max(pOCV)_{1,i} - max(pOCV)_{k,i}}{max(pOCV)_{1,i}} \cdot 100 \\ \mathrm{LLI}_{IC-DV,k,i}(\%) = \dfrac{abs(max(Q_1))_i - abs(max(Q_k))_i}{abs(max(Q_1))_i} \cdot 100 \\ \mathrm{LAM}_{IC-DV,k,i}(\%) = \dfrac{abs\left(max\left(\frac{\Delta Q}{\Delta pOCV_1}\right)\right)_i - abs\left(max\left(\frac{\Delta Q}{\Delta pOCV_k}\right)\right)_i}{abs\left(max\left(\frac{\Delta Q}{\Delta pOCV_1}\right)\right)_i} \cdot 100 \end{cases} \tag{6}$$

For $k = 1 \ldots 11$, $i = 1 \ldots 4$.

These equations are used in Section 6.2 to quantify the effects of DMs based on the IC-DV technique.

4. Experimental procedure

This study uses the experimental data collected in Ref. [3] where four 3 Ah 18650 NCA-C Li-ion cells connected in parallel were cycled until their End of Life (EoL). The EoL corresponds to 500 cycles based on a measure of capacity fade. Before being connected in parallel each cell was individually aged by 0, 50, 100 and 150 cycles (refer to Section 4.1) to emulate an imbalanced scenario, i.e. the SoH of each cell connected in parallel is different. The maximum SoH cell-to-cell difference (150 cycles) corresponds to a difference of capacity and impedance of circa 8% and 30%, respectively. Research published highlights that differences in cell properties from initial manufacture and integration may be circa 9% for capacity and 25% for impedance [3]. The values are in agreement with the initial differences considered in this study.

A full description of the experimental procedure is provided in Ref. [3] and will therefore not be duplicated here. For completeness however, a summary, highlighting pertinent aspects of the test programme, are provided for reference.

The experimental procedure is divided into two phases: cycle ageing and cell characterisation. Table 4 provides an overview of the test and following subsections summarise the procedures.

4.1. Cycle ageing

Fig. 2 (a) shows one cycle which was undertaken repeatedly at constant ambient temperature of 25 °C ± 1 °C. The cycle consisted of a Constant Current-Constant Voltage (CC-CV) charge followed by a 1 C constant discharge until the lower voltage was reached (2.5 V). The CC phase involved charging the cell at C/2 until the end of charge voltage (4.2 V) was reached. The CV phase then consisted of charging the cell at 4.2 V until the current fell to C/20 (150 mA). Full DoD (e.g. from 0% to 100% and back to 0%) without using large currents [3] enables the cells to be significantly aged without exceeding the manufacturers operating cell

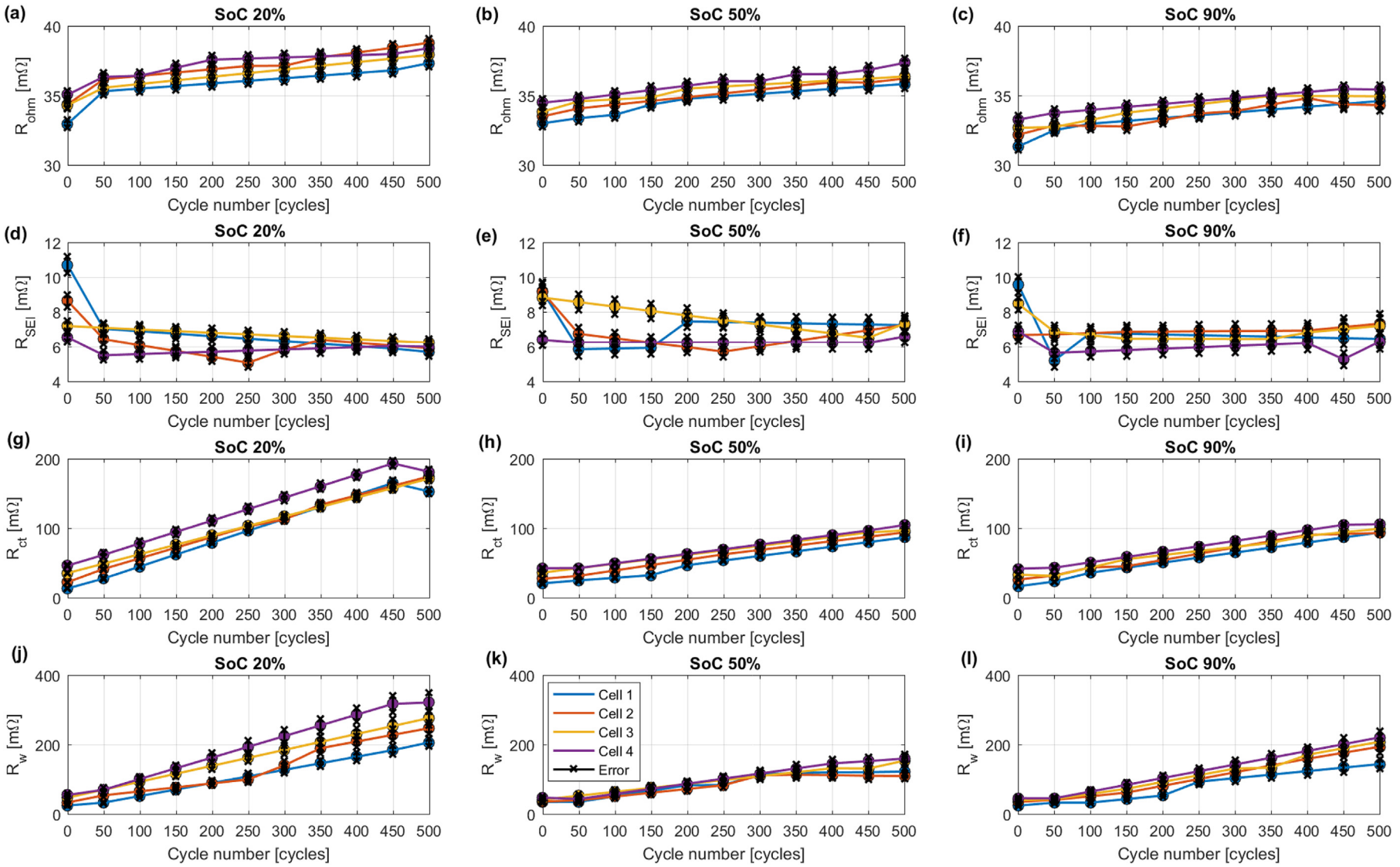

Fig. 3. (a)–(c) R_{ohm}, (d)–(f) R_{SEI}, (g)–(i) R_{ct}, (j)–(l) R_W fitting results and error band at SoC 20%, SoC 50% and SoC 90% over cycle number.

specification. A large DoD is conceived to emulate the operation of a typical BEV in which, as discussed within [3], the BMS will control a large variation in SoC to further maximise the range of the vehicle.

4.2. Cell characterisation

Cell characterisation includes three tests: capacity test, pOCV test and EIS test. This study only uses the data of the pOCV and EIS tests and therefore only these tests are here described. In order to track the aged state of each cell over time, each of these tests were performed after every 50 cycles. In total, each cell was characterised 11 times during the course of the experimental programme. To ensure that the change of the AR-ECM parameters (EIS) and the changes of the IC-DV curves is due to ageing rather than to the variation of the extrinsic factors (e.g. temperature, SoC, ΔDoD and C-rate), the characterisation tests were performed consistently at the same conditions for the entire duration of the experiment.

- The pOCV test comprises measuring the cell terminal voltage as it no load (zero current) would be connected. The pOCV test was performed by discharging from the cell upper voltage threshold (4.2 V) to the cell lower voltage threshold (2.5 V) at C/10. Fig. 2 (b) illustrates the pOCV against the SoC. The SoC was calculated as the integral of the current and normalised with respect to the capacity of the cell.
- The EIS test used a Solartron modulab system (model 2100A) in galvanostatic mode (i.e. current is controlled) with a peak current amplitude of 150 mA (C/20). The tests were performed between 2 mHz and 100 kHz at SoC = 20%, SoC = 50% and SoC = 90%. The SoC was adjusted by setting the appropriated pOCV value obtained from Fig. 2 (b). As an example, Fig. 2 (c) illustrates the EIS spectra for cell 1 at 0 cycle (i.e. the beginning of this test), covering the frequency range that a BMS typically operates (<100 Hz) and the corresponding measured resistance, R_{BMS} [3]. According to [36], a period of 4 h rest was allowed prior to performing each EIS test. This rest period avoids changes in the internal impedance after the cells are excited. It is also worth mentioning the importance of proper connection of the cells to the EIS test system as inaccurate EIS measurements can easily result from poor connections.

5. Experimental results

5.1. EIS

The AR-ECM was fitted to the EIS measurements using the complex non-linear least squares algorithm (CNLS). The fitting routine was completed with the Z$_{view}^{©}$ software package [31]. The

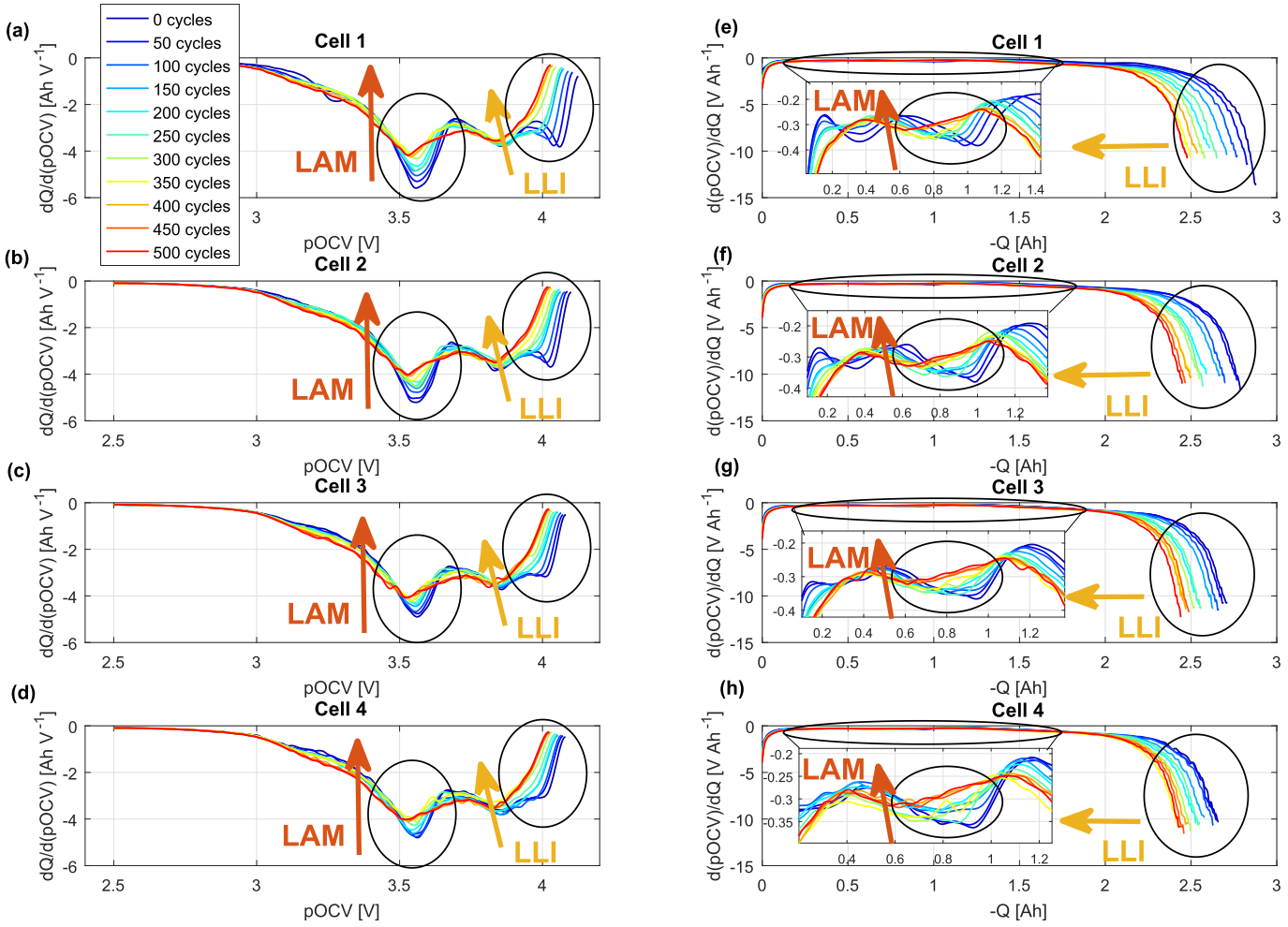

Fig. 4. (a)–(d) IC and (e)–(h) DV discharge curves for each cell over cycle number. The changes of the IC and DV curves are related to the most pertinent DM according to Table 3.

maximum difference between the fitted model response and the EIS measurements (maximum fitted error) was 10%. Fig. 3 shows the values of ohmic resistance (R_{ohm}), SEI resistance (R_{SEI}), charge-transfer resistance (R_{ct}) and Warburg resistance (R_W) obtained from the fitting process along with their error band. Fig. 3 shows that R_{ohm} and R_{SEI} increases less than R_{ct} and R_W.

5.2. IC-DV

Fig. 4 shows the IC and DV curves for each cell and the effect of the DMs evolution with number of cycles. The height of the IC peaks decreases at an approximately constant V_{poc} over cycle number as a measure of the effects of LAM. This reduction of the height of the IC peaks is also manifested in a decrease in the magnitude of the depths of the valleys at an approximately constant charge in the DV curves. This study considers the reduction of the height of the peaks in the IC curves to calculate the growth of the effects of LAM because their variation is clearer than the reduction of the depths of the valleys in the DV curves. The shift towards lower capacities in the DV curves indicates the effect of LLI. This shift toward lower capacities is also observable as a decrease of the height of the IC peaks toward lower voltages as described in Section 3.4. Similar as to the LAM, this study considers the shift toward lower capacities in the DV curves to calculate the growth of the effects of LLI because their variation can be observed clearer than the decrease of the height of the IC peaks toward lower voltages. For the case of CL, neither constant reduction of V_{poc} (IC) nor lack of change of capacity (DV) is observed and therefore, the effects of CL are negligible using the IC-DV technique.

6. Discussion

6.1. Analysis of degradation modes using EIS

The increase of the DMs observed through EIS is quantified by the change of each AR-ECM resistance (R_{ohm}, R_{SEI}, R_{ct} and R_W) shown in Equation (2). Fig. 5 shows that the growth of the effects of LLI and the growth of the effects of LAM are larger than the growth of the effects of CL over cycle number, for each cell and SoC. This result is due to R_{ct} (LLI) and R_W (LAM) increasing more than R_{ohm} (CL) as the cell ages. Based on the operating conditions at which the cells were cycled (ΔDoD = 100%, 1 C discharge, C/2 discharge and 25 °C) the effect of these DMs are consistent with the theoretical expectations (refer to Section 2).

For most of the cells and SoCs the growth of LLI and the growth of LAM follows a linear trend over cycle number. This result is supported by the linear increase of the resistance seen in other studies [37,38].

6.2. Analysis of degradation modes using IC-DV

The shifting of the IC and DV curves enables the quantification of the effects of the DMs using Equation (6). Fig. 6 illustrates the growth of the effects of LLI and the growth of the effects of LAM linearly increases from 0 cycles to 400 cycles and then a plateau is reached until 500 cycles (end of the experiment). This trend is different with respect to the trend obtained for the EIS case where the growth of the effects of the DMs increases linearly. This relies on the fact that generally the measures behind EIS and IC-DV change

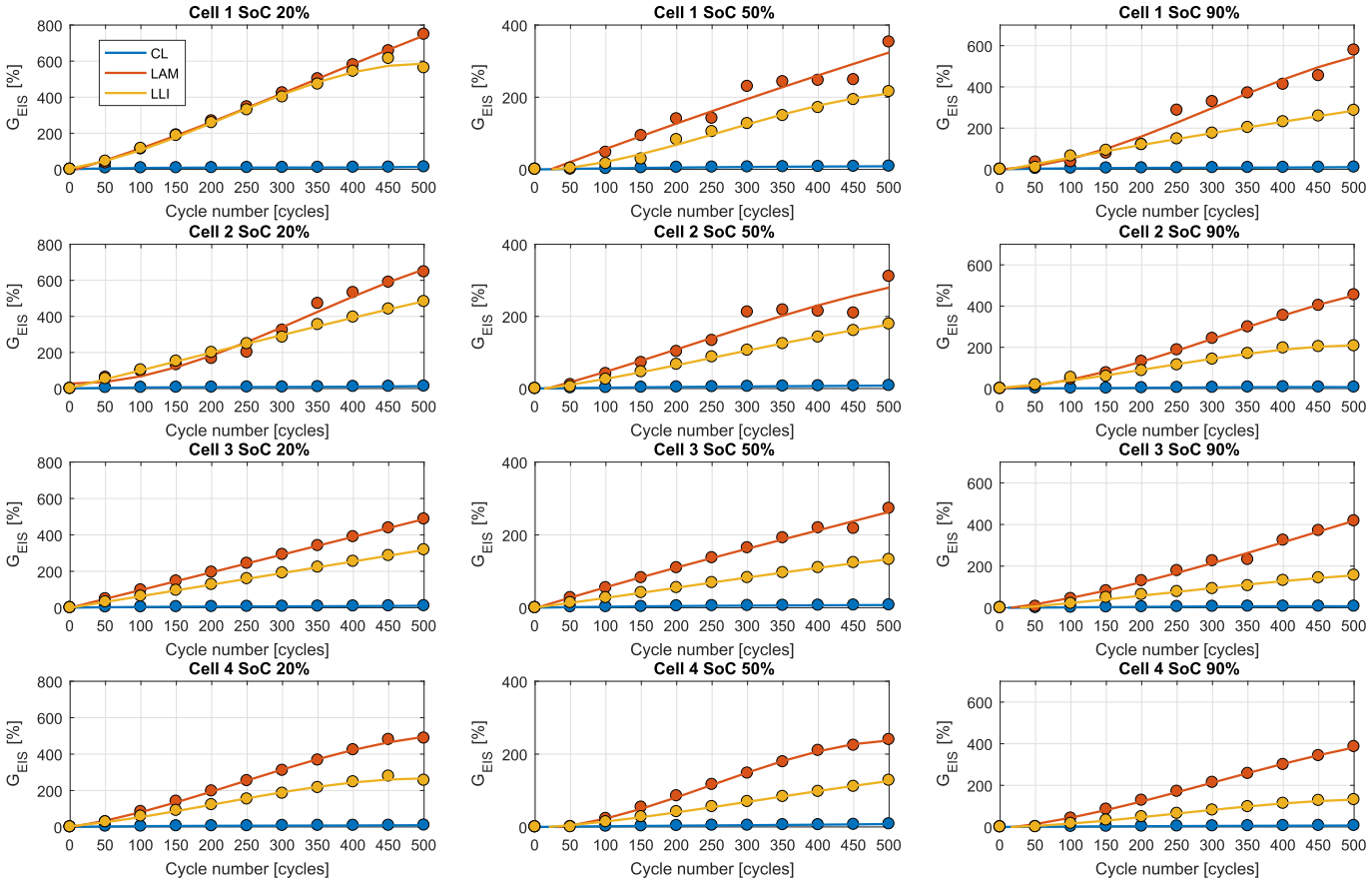

Fig. 5. G_{EIS} for each DM for every cell at SoC 20%, SoC 50% and SoC 90% over cycle number.

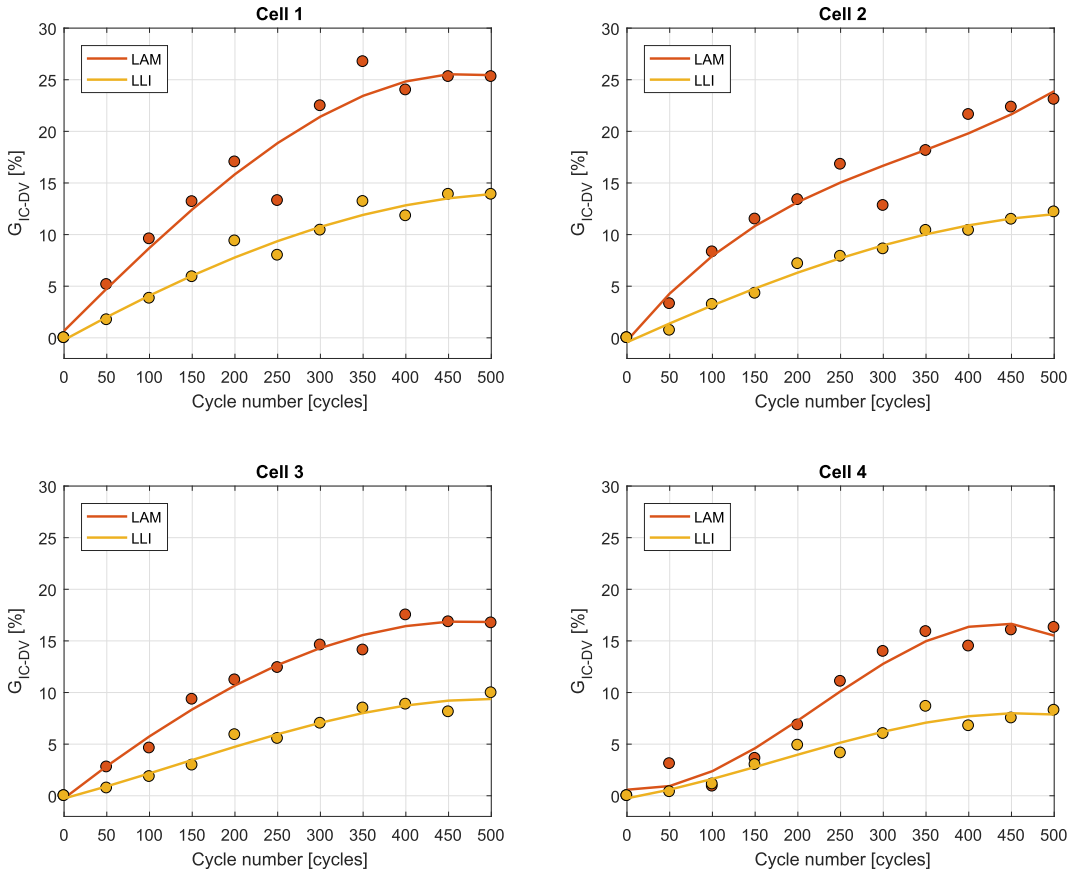

Fig. 6. G_{IC-DV} for each DM for every cell over cycle number.

differently, i.e. resistance increases linearly (EIS case) and capacity decreases closer to an exponential trend (IC-DV case) with ageing as reported in Ref. [3]. From these results it is also seen the growth of the effects due to CL are neglected using IC-DV curves. This is in agreement with the results obtained using the EIS where the growth of the effects due to CL (13.4%) are significantly lower in comparison to the growth of the effects due to LLI (614%) and LAM (748%) (refer to Fig. 5).

6.3. SoC dependency

Fig. 7 shows the effect of LLI and LAM over cycle number is larger for SoC 20% than for SoC 50% and 90%. This suggests that charge-transfer and Warburg resistances increase more for SoC 20% than for SoC 50% and SoC 90% through ageing. This result is corroborated by Huang et al. [39] for the case of NMC chemistry when the cells are new. Pietsch et al. [40] observed that lithiation kinetics within graphite electrodes are limited by ionic diffusion and conductivity rather than by electric conductivity. In addition, Huang et al. [39] suggest that the increase of the Warburg resistance can be explained based on the diffusion coefficient and the concentration of the reactants for both positive and negative electrodes. Thus, the variation of the ionic diffusion and conductivity would need to be measured through ageing with respect to the level of lithiation (SoC) for the positive and negative electrodes. Such a measurement may highlight the reasons of the larger increase of charge-transfer and diffusion resistances at SoC 20%. Measurement of these parameters are beyond of the scope of this study and further work is required with this respect.

6.4. Evaluation of DMs with respect to cell-to-cell dependency

Fig. 8 shows the effects of the DMs obtained with EIS and IC-DV follow a relationship with respect to the initial level of ageing of each cell, i.e. the growth of the effects of each DM is more pertinent for the less aged cells than for the more aged cells as reported in Ref. [3]. The cells that initially have aged less degrade faster than the cells that initially have aged more because the charge throughput of the less aged cells are larger than the charge-throughput of the more aged cells [3].

6.5. Comparison between EIS and IC-DV technique

EIS and IC-DV techniques highlighted that the effects of LAM and LLI are more significant than the ageing effects attributable to CL. This agrees with previous studies [24–29] where the related ageing mechanisms of commercial NCA-C cells were analysed for storage and cycling operation. The growth of the effect of each DM differs greatly between EIS (from 0% to 800%) and IC-DV (from 0% to 30%). To compare the results obtained with EIS and IC-DV each DM metric is first normalised, $G_{n,EIS}$ and $G_{n,IC-DV}$, and then correlated to one another. For the case of IC-DV the degradation effect due to CL is neglected and hence, this is not considered in this comparison. The Pearson product-moment correlation coefficient (PPMCC) is employed to quantify the degree of correlation between G_{EIS} and G_{IC-DV}. The PPMCC coefficients are computed as the covariance divided by the standard deviations of each parameter using Equation (7) [41].

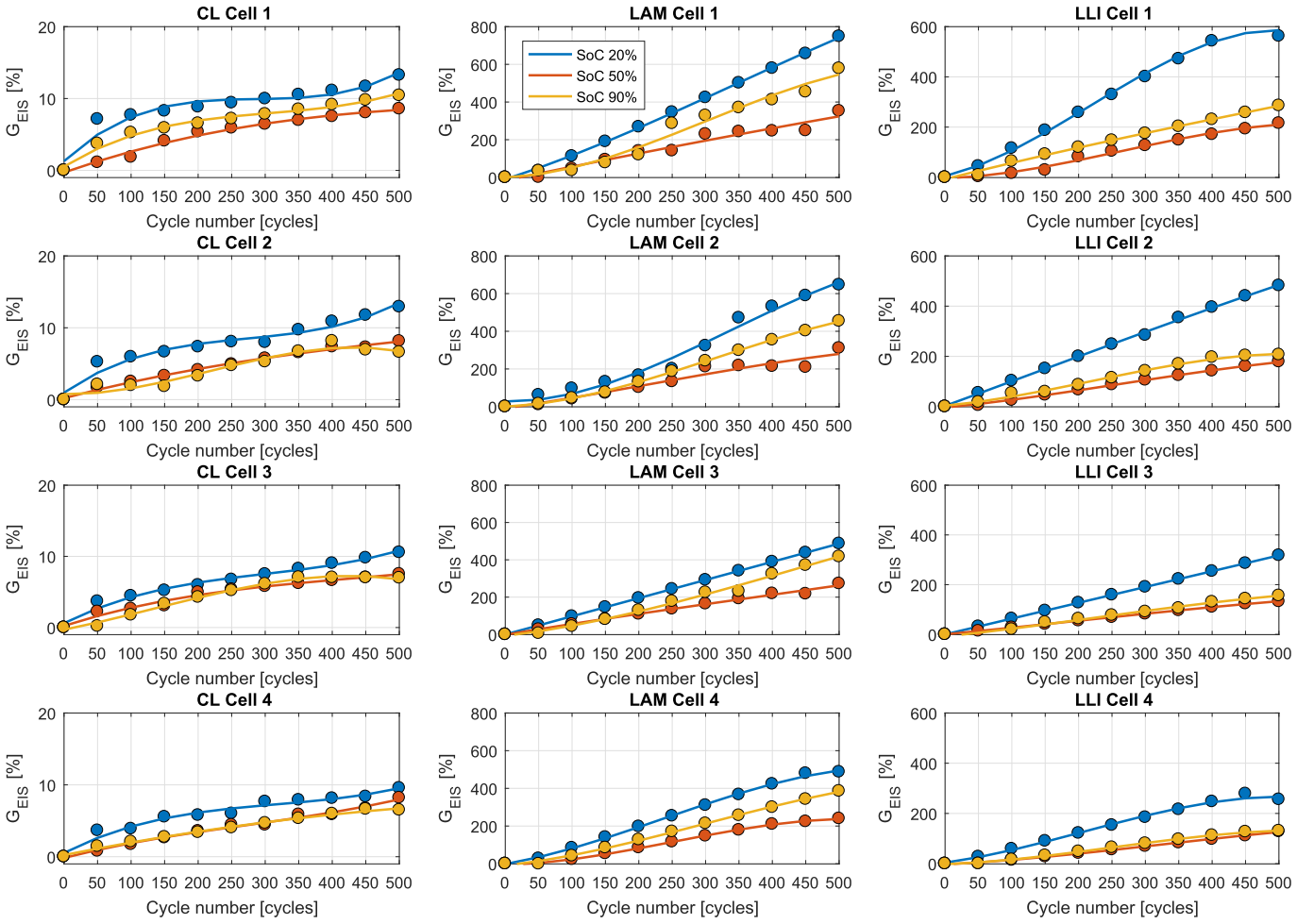

Fig. 7. Dependency of G_{EIS} with respect to SoC for each cell over cycle number.

$$r_{G_{n,EIS},G_{n,IC-DV}} = \frac{cov_{G_{n,EIS},G_{n,IC-DV}}}{\sigma_{G_{n,EIS}} \cdot \sigma_{G_{n,IC-DV}}} \tag{7}$$

The PPMCC varies between 0 and ±1, depending whether the correlation is weak (0) or strong (±1). The paired-sample *t*-test is then employed to calculate the probability (p-value) that the correlation between $G_{n,EIS}$ and $G_{n,IC-DV}$ is significant. The paired t-value as a function of *r* and the sample size *n* is computed using Equation (8).

$$t = \frac{r \cdot \sqrt{n-2}}{2 \cdot \sqrt{1-r^2}} \tag{8}$$

This equation is the same as the one used for the one-sample *t*-test [41] but adapted to the paired-sample *t*-test. The difference between both relies on the number of degrees of freedom, i.e. n-2 is the number of degrees of freedom for the one-sample *t*-test and n-1 is the number of degrees of freedom for the paired-sample *t*-test.

Before applying the paired *t*-test, the sample data must fulfill the following requirements [41]:

- The dependent variable must be measured in a continuous scale. $G_{n,EIS}$ and $G_{n,IC-DV}$ are continuous measurements because they can take any value within a range between 0 and 1.
- The sample data is normally distributed. This check is performed employing the chi-square goodness of fit test, using the *chi2gof* command within MATLAB©. The result of this test was that the sample data $G_{n,EIS}$ and $G_{n,IC-DV}$ follow a normal distribution for each cell and SoC.
- The observations need to be dependent. Since the observations quantifies the effect of the DMs they are dependent.
- There should be no significant outliers. Box plots were generated for each data set showing the absence of outliers. This check is performed using the *boxplot* command in MATLAB©.

As these requirements are fulfilled, the paired-sample *t*-test is applied to each data-set. For every cell three DMs are defined and for each DM there are three different data-sets since EIS includes measurements at SoC 20%, 50% and 90%. For each SoC the same $G_{n,IC-DV}$ is considered. The PPMCC values and the p-values of the paired *t*-test are computed using *corrcoef* and *ttest* commands in MATLAB©, respectively. Table 5 shows the p-values for each cell, SoC and DM. In addition, the p-values were also computed for the case that the data of all cells is considered. For all the cases evaluated the p-value is lower than 0.05 and so $G_{n,EIS}$ and $G_{n,IC-DV}$ are significantly correlated. Neglecting the degradation effect due to CL which is not identifiable with IC-DV technique, this result highlights that EIS and IC-DV identifies and quantifies the same effects of DMs at the same level (LLI and LAM). From this it can be also concluded that the effects of the DMs lead in the same order to capacity fade and power fade.

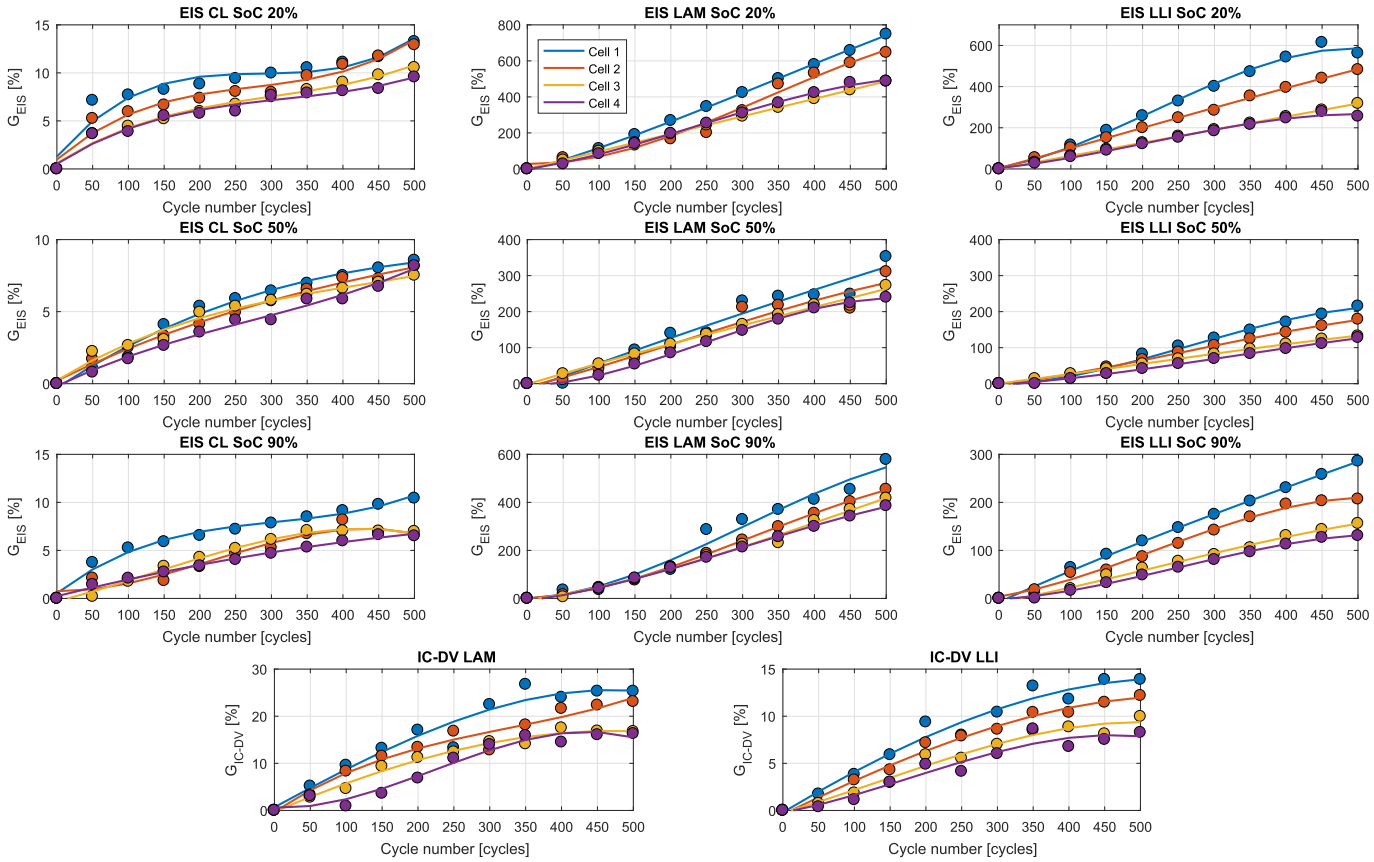

Fig. 8. Cell-to-cell dependency of the effects of the DMs over cycle number.

Table 5
p-values for each cell, SoC and DM derived from the *t*-test.

Cell	LLI			LAM		
	SoC 20%	SoC 50%	SoC 90%	SoC 20%	SoC 50%	SoC 90%
1	0.0030	0.0334	0.0034	0.0029	$4.7559\cdot10^{-4}$	0.0027
2	0.0011	0.0060	0.0013	0.0082	0.0064	0.0024
3	0.0014	0.0011	0.0083	0.0026	0.0015	8.4366e-04
4	$6.7165\cdot10^{-4}$	0.0123	0.0053	0.0148	0.0236	0.0123
All	$3.9748\cdot10^{-13}$	$1.7939\cdot10^{-11}$	$4.8669\cdot10^{-12}$	$7.1977\cdot10^{-12}$	$1.1047\cdot10^{-11}$	$2.0279\cdot10^{-10}$

6.6. Implications for future battery pack designs

Within a typical BMS application, the BMS currently monitors battery pack performance and quantifies SoH through the calculation of a single number or percentage without providing any indication of the root causes of battery ageing (DMs). Identification and quantification of the effects of the DMs by a BMS under real operating conditions can be feedback to improve lifetime control strategies and the manufacturing and design processes of batteries so that the impact of intrinsic and extrinsic factors on battery ageing will be ultimately reduced. It is shown that the degradation effects due to LAM and LLI are the most pertinent in this study. Relating this with Table 1, the increase in the effects of LAM is accelerated due to high cycle number and a large ΔDoD and the growth of the effects of LLI is enhanced due to a large ΔDoD. Crystal structural disorder, intercalation gradient strains in the active particles (LAM), solvent co-intercalation (LAM and LLI) and growth of NiO-like structure layer (LLI) are identified as the main ageing mechanisms whose effects need to be limited, e.g. through appropriate manufacturing, design or BMS lifetime control strategies. For instance, an intercalation gradient strain in the active particles leads to volume change [1]. A battery design improvement would be to use robust polymeric binders (e.g. alginate binder) so that volume expansion (i.e. mechanical fracture of the electrodes) can be mitigated during cycling [42].

The BMS can also mitigate the impact of extrinsic factors on battery pack degradation. Some strategies could be for instance through limiting the excitation current under low and high temperature conditions, reducing the allowable DoD of the battery or changing the charging strategy.

The requirements to implement EIS and IC-DV on-board within a BMS are different. EIS measurements are performed using low amplitude voltage or current signals to avoid exciting the non-linear impedance characteristics of the cell. However, these low amplitude signals can be easily perturbed by noise and so the corresponding impedance measurement may not be accurate. Thus, achieving a good Signal to Noise Ratio (SNR) is a challenge [16]. Another aspect to consider is the requirement for a time

invariance so that the SoC is kept constant along the measurement [16]. In addition, the EIS spectra in this case covers a range of frequencies from 2 mHz to 100 kHz that a low-cost BMS microcontroller cannot currently support since their maximum operating frequencies are typically only up to 100 Hz [3]. To overcome this, few authors [16,17] have proposed a low cost impedance measurement system using the current signal of the DC converter to excite the battery across a wide range of frequencies.

For the IC-DV, the cells need to be discharged or charged at constant C-rate (≤C/10) to ensure the battery is at equilibrium. Real-driving scenarios make the discharge operation of batteries significantly dynamic and therefore the IC-DV technique could be only applied on-board when the battery is charged slowly at low and constant C-rate (≤C/10). This implies the minimum charging time would be at least 10 h. This is feasible if the parking time for PHEVs and BEVs, when their LIBs are charged overnight, is at least 10 h or if the customer set the departure time allowing at least 10 h of charging [43]. Performing this test would be in practice easily scheduled because ageing processes in LIBs are slow and so the effects of the DMs do not need to be quantified regularly (e.g. twice per year) [44].

An alternative to quantify DMs without using EIS and pOCV measurements would be to predict the AR-ECM and the pOCV curve using estimation algorithms as proposed in Refs. [45,46].

Apart from measuring or estimating the EIS and pOCV data, the fitting procedure based on CNLS algorithm (EIS), and filtering and differentiation techniques used to smooth the IC-DV curves do not require excessive computation demand and memory, and therefore both techniques could be implemented in a low-cost microcontroller without incurring significant penalty of requiring additional hardware resources.

The decision of which technique to implement within a BMS depends on a number of factors. Table 6 summarises advantages and disadvantages of each technique so that it is possible to asses quickly which technique would be better for a particular case. Computationally, IC-DV is simpler to implement within a BMS than EIS because IC-DV is model independent and it demands less calculations. The filtering and differentiation procedure (e.g. number and complexity of the equations to be solved) is less computationally demanding than the fitting procedure used when correlating EIS spectra to a representative ECM. However, the test required to acquire the data for the IC-DV curves is generally longer than for the EIS (assuming the lower frequency employed for the data capture is 2 mHz as in this case). In addition, EIS enables quantification of the effects of the DMs at a particular SoC whilst IC-DV curves are determined along the whole SoC window. In line with this, EIS seems to provide a better resolution of the DMs than the IC-DV curves. For instance, in this case EIS enables the identification of the effect of CL whilst IC-DV curves neglect the effect of it. It is recommended therefore to apply both techniques since each one have different advantages and disadvantages. In addition, each technique considers a different degradation parameter (capacity and resistance) which may also infer different DMs.

7. Limitations of this study and further work

Although the results of this study are valid for the described experimental conditions, the authors postulate that the underlying framework, tools and reasoning presented is transferable to other cell technologies and ambient conditions. In cases where the environmental and usage conditions change (e.g. ambient temperature, C-rate); or, the number of cells connected in parallel is different; or, the conditions at which the cells were initially aged vary; then, the type of AR-ECM (for the EIS case), the analysis of the effects of the DMs, and their SoC and cell-to-cell dependency may be different. For instance, if the same experiment is run at lower temperatures ($T < 5\ ^{\circ}C$) and high currents ($C_{rate} > 2C$) the cells may be subjected to lithium plating causing a larger increase of the effects due to LLI (refer to Table 1). Hence, the similarity of the results obtained and the applicability of the EIS and IC-DV should also be investigated over a broader range of conditions (storage or dynamic cycling at different C-rates, constant operation at low, mid and high SoC, low and high temperature, and shallow ΔDoD), and for other cell chemistries, formats and manufacturers. Such investigations will also confirm the relationship between extrinsic factors, DMs and ageing mechanisms (summarised in Table 1) when different operating conditions exist.

With regards to EIS and DMs interpretation, the authors acknowledge that Schindler et al. [32] found a similar correlation between EIS resistances and LLI and LAM. They relate R_{ohm} with LLI, and R_{ct} and R_W with LAM, which differs with our arguments. Therefore, further work to clarify the validity of each argument is needed.

Classifying the different ageing mechanisms into CL, LLI and LAM can be misleading. For example, Fig. 3 shows that the predominant contribution to power fade occurs due to increase in R_{ct} and R_W. This is consistent with the theory of battery degradation (refer to Table 1). However, within the LLI, LAM and CL framework there is no obvious way to express that resistance rise and power fade are the principal mode and effect of degradation. Similarly, within this framework the main degradation mode for SEI is LLI (refer to Table 1). This is controversial with respect to previous literature [5,26], which state that power fade is the main result of SEI growth and not LLI. In summary therefore, categorising DMs as suggested in Refs. [2,4,22,47] and corroborated in this study is limited and in some cases can be misleading. To quantify such inaccuracy and validate the results obtained alternative in-situ diagnosis techniques such as DTV [10,11] and ex-situ post-

Table 6
Advantages and disadvantages of EIS and IC-DV.

Technique	Advantages	Disadvantages
EIS	(a) Quick test duration (25 min/cell). (b) Possible for on-board implementation subject to SNR and time invariance. (c) Enable measurements at particular frequencies and SoC.	(a) Accuracy dependent on different sources: measurements and model. (b) Complex computation (requires fitting a model). (c) Not universal (model dependent).
IC-DV	(a) Accuracy dependent mostly on the measurement (C-rate used). (b) Possible for on-board implementation subject to charge/discharge C-rate. (c) Simple calculation. (d) Universal (model independent).	(a) Long test duration (10 h/cell). (b) Do not enable measurements at particular frequencies and SoC. (c) The effect of some DMs can be neglected (e.g. CL).

mortem analysis such as SEM, EDS or XRD [12] should be used. In line with this, further work also includes to isolate and quantify the effects of different DMs resulting from the same ageing mechanism. In addition, the effects of DMs change with respect to the SoC through ageing. The measurement of the ionic conductivity and diffusion in the positive and negative electrodes may explain the variation of the effects of DMs with respect to SoC through ageing and thus, further work is required with this respect.

This work suggests the potential implementation of EIS and IC-DV techniques on-board in a commercial BMS. However, a more detailed study is required with this respect. The accuracy and robustness of these methods in such environment needs to be evaluated as a further work.

In order to reduce the duration of the experiment only one cell capacity and resistance measurement was considered. According to the theory of Design of Experiments (DoE) [3], more than one sample is recommended to ensure the measurements are representative of the whole population. Thus, a greater sample size is necessary to increase confidence in the findings of this study.

8. Conclusions

This study proposes a robust method to identify and quantify the effects of DMs in Li-ion batteries using EIS and IC-DV diagnostic techniques. Using either EIS or IC-DV, LLI and LAM are identified to be the most pertinent DMs. Furthermore, the results obtained via each technique are significantly correlated at a confidence interval of 95%, suggesting that both techniques are suitable for identification and quantification of the effects of the DMs. However, each of these techniques has its own advantages and drawbacks for implementation in a commercial BMS. It is therefore worth to investigating both simultaneously as on-board diagnostics tools. Additionally, each technique uses a different parameter (capacity or resistance) to quantify ageing and can therefore be used to infer different DMs.

The change in the effect of the DMs was also analysed with respect to SoC and the different amount of degradation of each cell. The growth of the effects in terms of LAM and LLI is larger at 20% SoC than at 50% and 90% SoC. The effect of the DMs changes as a function of the initial degradation of each cell connected in parallel, i.e. the effects of the DMs are higher for the less aged cells than for the more aged cells. This result is due to the charge-throughput is larger in the less aged cells than in the more aged cells, as reported in Ref. [3].

Different sources of variation (extrinsic or intrinsic factors) can have an effect on the ideal battery function leading to accelerated ageing. These stress factors affect the ideal functionality of cells such that various ageing mechanisms are cause-triggered. Improving manufacturing processes quality control or appropriate selection of the cell materials would limit the impact of intrinsic factors. In line with this, identification and quantification of the effects of DMs through a BMS under real operating conditions will support the selection of the most appropriate cell materials, topology, design and manufacturing processes, so that the effect of ageing mechanisms can be reduced.

Similarly, the BMS can mitigate the impact of the extrinsic factors to the extend that cell performance (range and power) is not affected by performing an appropriate control of the temperature, C-rate, SoC and ΔDoD.

Acknowledgements

The research presented within this article is supported by the Engineering and Physical Science Research Council (EPSRC - EP/I01585X/1) through the Engineering Doctoral Centre in High Value, Low Environmental Impact Manufacturing. The research was undertaken in the WMG Centre High Value Manufacturing Catapult (funded by Innovate UK) in collaboration with Jaguar Land Rover. Details of additional underlying data in support of this article and how interested researchers may be able to access it can be found here: http://wrap.warwick.ac.uk/87247. The authors would like also to thank Dr. Mark Tucker, Dr. Hin Kwan Wong and Thomas Bruen for their support on the analysis of the results.

Nomenclature

Abbreviation

AR-ECM	Adapted Randles - Equivalent Circuit Model
BMS	Battery Management System
BEV	Battery Electric Vehicle
BoL	Begin of Life
Charact.	Characterisation
CC	Current Collector
CC	Constant Current
CF	Capacity Fade
CL	Conductivity Loss
CNLS	Complex Non-Linear Least Squares
CPE	Constant Phase Element
CV	Constant Voltage
DoD	Depth of Discharge
DTV	Differential Thermal Voltammetry
ECM	Equivalent Circuit Model
EDS	Energy Dispersive Spectrometry
EIS	Electrochemical Impedance Spectroscopy
EoL	End of Life
IC-DV	Incremental Capacity and Differential Voltage
LAM	Loss of Active Material
LIB	Lithium-ion Battery
LLI	Loss of Lithium Inventory
NCA-C	Lithium Nickel Cobalt Aluminum - Carbon, $LiNi_xCo_{1-x-y}Al_yO_2$
NCM	Nickel Cobalt Manganese, $LiNiMnCoO_2$
PHEV	Plug Hybrid Electric Vehicle
pOCV	Pseudo Open Circuit Voltage
PF	Power Fade
SEI	Solid Electrolyte Interphase
SEM	Scanning Electron Microscopy
SoC	State of Charge
SoH	State of Health
SoH_E	State of Health based on capacity
SoH_P	State of Health based on resistance
SPI	Solid Permeable Interphase
XRD	X-Ray Diffractometer

Symbol Description, Unit

C	Capacity, [Ah]
$(Number)C$	C-rate, [A]
cov	Covariance, [−]
f	frequency, [Hz]
F	Faraday constant (96485.33), [As mol^{-1}]
G	Growth of degradation, [%]
L	Inductance, [H]
l	specific diffusion thickness, [mm]
n	phase angle coefficient, [−]
p	p-value, [−]
Q	Charge, [Ah]
R	Resistance, [Ω]
r	Pearson product-moment correlation coefficient, [−]
T	Temperature, [°C]

t	t-value (t-test), [−]
V	Voltage signal, [V]
#	Number of, [−]
σ	Standard deviation, [−]

Indices

ct	Charge-transfer
dl	double layer
i	Cell number
k	Characterisation test
now	Present value
oc	Open circuit value (voltage)
Ohm	Ohmic
poc	Pseudo open circuit value (voltage)
q	SoC value (20%, 50% or 90%)
SEI	Solid Electrolyte Interphase
samp	Sampling
t	Terminal value (voltage)
W	Warburg

References

[1] K. Uddin, S. Perera, W. Widanage, L. Somerville, J. Marco, Characterising lithium-ion battery degradation through the identification and tracking of electrochemical battery model parameters, Batteries 2 (2) (2016) 13, http://dx.doi.org/10.3390/batteries2020013.

[2] M. Dubarry, A. Devie, B.Y. Liaw, The value of battery diagnostics and prognostics, J. Energy Power Sources 1 (5) (2014) 242–249.

[3] C. Pastor-Fernández, T. Bruen, W. Widanage, M. Gama-Valdez, J. Marco, A study of cell-to-cell interactions and degradation in parallel strings: implications for the BMS, J. Power Sources 329 (2016) 574–585, http://dx.doi.org/10.1016/j.jpowsour.2016.07.121.

[4] M. Dubarry, C. Truchot, B.Y. Liaw, Synthesize battery degradation modes via a diagnostic and prognostic model, J. Power Sources 219 (2012) 204–216, http://dx.doi.org/10.1016/j.jpowsour.2012.07.016.

[5] J. Vetter, P. Novák, M.R. Wagner, C. Veit, K.C. Möller, J.O. Besenhard, M. Winter, M. Wohlfahrt-Mehrens, C. Vogler, A. Hammouche, Ageing mechanisms in lithium-ion batteries, J. Power sources 147 (1–2) (2005) 269–281, http://dx.doi.org/10.1016/j.jpowsour.2005.01.006.

[6] C. Pastor-Fernández, W.D. Widanage, G.H. Chouchelamane, J. Marco, A SoH diagnosis and prognosis method to identify and quantify degradation modes in Li-ion batteries using the IC/DV technique, in: 6th Hybrid and Electric Vehicles Conference (HEVC 2016), 2016, pp. 1–6, http://dx.doi.org/10.1049/cp.2016.0966.

[7] Y. Zhang, C.-Y. Wang, Cycle-life characterization of automotive lithium-ion batteries with LiNiO[sub 2] cathode, J. Electrochem. Soc. 156 (2009) A527, http://dx.doi.org/10.1149/1.3126385.

[8] U. Tröltzsch, O. Kanoun, H.-R. Tränkler, Characterizing aging effects of lithium ion batteries by impedance spectroscopy, Electrochim. Acta 51 (8–9) (2006) 1664–1672, http://dx.doi.org/10.1016/j.electacta.2005.02.148.

[9] C. Pastor-Fernández, W.D. Widanage, J. Marco, M.Á. Gama-Valdez, G.H. Chouchelamane, Identification and quantification of ageing mechanisms in Lithium-ion batteries using the EIS technique, in: 2016 IEEE Transportation Electrification Conference and Expo (ITEC), 2016, pp. 1–6, http://dx.doi.org/10.1109/ITEC.2016.7520198.

[10] Y. Merla, B. Wu, V. Yufit, N.P. Brandon, R.F. Martinez-Botas, G.J. Offer, Extending battery life: a low-cost practical diagnostic technique for lithium-ion batteries, J. Power Sources 331 (2016) 224–231, http://dx.doi.org/10.1016/j.jpowsour.2016.09.008.

[11] Y. Merla, B. Wu, V. Yufit, N.P. Brandon, R.F. Martinez-Botas, G.J. Offer, Novel application of differential thermal voltammetry as an in-depth state-of-health diagnosis method for lithium-ion batteries, J. Power Sources 307 (2016) 308–319, http://dx.doi.org/10.1016/j.jpowsour.2015.12.122.

[12] E. Sarasketa-Zabala, F. Aguesse, I. Villarreal, L.M. Rodriguez-Martinez, C.M. López, P. Kubiak, Understanding lithium inventory loss and sudden performance fade in cylindrical cells during cycling with deep-discharge steps, J. Phys. Chem. C 119 (2) (2015) 896–906, http://dx.doi.org/10.1021/jp510071d.

[13] C. Arcus, A Tale of 3 Battery Packs, Clean Technica, 2016. https://cleantechnica.com/2016/01/06/a-tale-of-3-battery-packs/2016/.

[14] D. Worwood, Q. Kellner, M. Wojtala, W.D. Widanage, R. MGlen, D. Greenwood, J. Marco, A new approach to the internal thermal management of cylindrical battery cells for automotive applications, J. Power Sources 346 (2017) 151–166.

[15] I.J. Gordon, S. Genies, G. Si Larbi, A. Boulineau, L. Daniel, M. Alias, Original implementation of Electrochemical Impedance Spectroscopy (EIS) in symmetric cells: evaluation of post-mortem protocols applied to characterize electrode materials for Li-ion batteries, J. Power Sources 307 (2016) 788–795, http://dx.doi.org/10.1016/j.jpowsour.2016.01.036.

[16] D.A. Howey, P.D. Mitcheson, S. Member, V. Yufit, G.J. Offer, N.P. Brandon, Online measurement of battery impedance using motor controller excitation, IEEE Trans. Veh. Technol. 63 (6) (2014) 2557–2566.

[17] E. Din, C. Schaef, K. Moffat, J.T. Stauth, A scalable active battery management system with embedded real-time electrochemical impedance spectroscopy, IEEE Trans. Power Electron. 32 (7) (2017) 5688–5698, http://dx.doi.org/10.1109/TPEL.2607519.

[18] C. Weng, Y. Cui, J. Sun, H. Peng, On-board state of health monitoring of lithium-ion batteries using incremental capacity analysis with support vector regression, J. Power Sources 235 (2013) 36–44, http://dx.doi.org/10.1016/j.jpowsour.2013.02.012.

[19] M. Berecibar, M. Garmendia, I. Gandiaga, J. Crego, I. Villarreal, State of health estimation algorithm of LiFePO4 battery packs based on differential voltage curves for battery management system application, Energy 103 (2016) 784–796, http://dx.doi.org/10.1016/j.energy.2016.02.163.

[20] H. Popp, J. Attia, F. Delcorso, A. Trifonova, Lifetime analysis of four different lithium ion batteries for (plug−in) electric vehicle, Transport Research Arena.

[21] Chemicool.com, Cobalt. URL http://www.chemicool.com/elements/cobalt.html%7b%25%7d3E.

[22] C.R. Birkl, M.R. Roberts, E. Mcturk, P.G. Bruce, D.A. Howey, Degradation diagnostics for lithium ion cells, J. Power Sources (2016) 1–35. http://epg.eng.ox.ac.uk/content/degradation-diagnostics-lithium-ion-cells.

[23] A.J. Smith, J.C. Burns, D. Xiong, J.R. Dahn, Interpreting high precision coulometry results on Li-ion cells, J. Electrochem. Soc. 158 (10) (2011) A1136–A1142, http://dx.doi.org/10.1149/1.3625232.

[24] J.W. Braithwaite, A. Gonzales, G. Nagasubramanian, S.J. Lucero, D.E. Peebles, J.A. Ohlhausen, W.R. Cieslak, Corrosion of LithiumIon battery current collectors, J. Electrochem. Soc. 146 (2) (1999) 448–456, http://dx.doi.org/10.1149/1.1391627.

[25] S. Bourlot, P. Blanchard, S. Robert, Investigation of aging mechanisms of high power Li-ion cells used for hybrid electric vehicles, J. Power Sources 196 (16) (2011) 6841–6846, http://dx.doi.org/10.1016/j.jpowsour.2010.09.103.

[26] M. Broussely, P. Biensan, F. Bonhomme, P. Blanchard, S. Herreyre, K. Nechev, R.J. Staniewicz, Main aging mechanisms in Li ion batteries, J. Power Sources 146 (1–2) (2005) 90–96, http://dx.doi.org/10.1016/j.jpowsour.2005.03.172.

[27] S. Watanabe, M. Kinoshita, K. Nakura, Comparison of the surface changes on cathode during long term storage testing of high energy density cylindrical lithium-ion cells, J. Power Sources 196 (16) (2011) 6906–6910, http://dx.doi.org/10.1016/j.jpowsour.2010.12.028.

[28] S. Watanabe, M. Kinoshita, T. Hosokawa, K. Morigaki, K. Nakura, Capacity fade of LiAlyNi1xyCoxO2 cathode for lithium-ion batteries during accelerated calendar and cycle life tests (surface analysis of LiAlyNi1xyCoxO2 cathode after cycle tests in restricted depth of discharge ranges), J. Power Sources 258 (2014) 210–217, http://dx.doi.org/10.1016/j.jpowsour.2014.02.018.

[29] S. Watanabe, M. Kinoshita, T. Hosokawa, K. Morigaki, K. Nakura, Capacity fading of LiAlyNi1xyCoxO2 cathode for lithium-ion batteries during accelerated calendar and cycle life tests (effect of depth of discharge in charge−discharge cycling on the suppression of the micro-crack generation of LiAlyNi1xyCoxO2 particl, J. Power Sources 260 (2014) 50–56, http://dx.doi.org/10.1016/j.jpowsour.2014.02.103.

[30] J. Landesfeind, J. Hattendorff, A. Ehrl, W.A. Wall, H.A. Gasteiger, Tortuosity determination of battery electrodes and separators by impedance spectroscopy, J. Electrochem. Soc. 163 (7) (2016) A1373–A1387, http://dx.doi.org/10.1149/2.1141607jes.

[31] Scribner Associates Incorporated, Help Document Zview Version 3.3b, 2011.

[32] S. Schindler, M.A. Danzer, A novel mechanistic modeling framework for analysis of electrode balancing and degradation modes in commercial lithium-ion cells, J. Power Sources (2017) 226–236, http://dx.doi.org/10.1016/j.jpowsour.2017.01.026 (in press).

[33] D.P. Abraham, S.D. Poppen, A.N. Jansen, J. Liu, D.W. Dees, Application of a lithium−tin reference electrode to determine electrode contributions to impedance rise in high-power lithium-ion cells, Electrochim. Acta 49 (26) (2004) 4763–4775, http://dx.doi.org/10.1016/j.electacta.2004.05.040.

[34] A. Barré, B. Deguilhem, S. Grolleau, M. Gérard, F. Suard, D. Riu, A review on lithium-ion battery ageing mechanisms and estimations for automotive applications, J. Power Sources 241 (2013) 680–689, http://dx.doi.org/10.1016/j.jpowsour.2013.05.040.

[35] M. Dubarry, B.Y. Liaw, M.-S. Chen, S.-S. Chyan, K.-C. Han, W.-T. Sie, S.-H. Wu, Identifying battery aging mechanisms in large format Li ion cells, J. Power Sources 196 (7) (2011) 3420–3425, http://dx.doi.org/10.1016/j.jpowsour.2010.07.029.

[36] A. Barai, W.D. Widanage, J. Marco, A. Mcgordon, P. Jennings, A study of the open circuit voltage characterization technique and hysteresis assessment of lithium-ion cells, J. Power Sources 295 (2015) 99–107, http://dx.doi.org/10.1016/j.jpowsour.2015.06.140.

[37] S.F. Schuster, T. Bach, E. Fleder, J. Müller, M. Brand, G. Sextl, A. Jossen, Nonlinear aging characteristics of lithium-ion cells under different operational conditions, J. Energy Storage 1 (2015) 44–53, http://dx.doi.org/10.1016/j.est.2015.05.003.

[38] J. Groot, M. Swierczynski, A.I. Stan, S.K. Kær, On the complex ageing characteristics of high-power LiFePO4/graphite battery cells cycled with high charge and discharge currents, J. Power Sources 286 (2015) 475–487, http://dx.doi.org/10.1016/j.jpowsour.2015.04.001.

[39] Q.-A. Huang, Y. Shen, Y. Huang, L. Zhang, J. Zhang, Impedance characteristics

and diagnoses of automotive lithium-ion batteries at 7. 5 % to 93. 0 % state of charge, Electrochim. Acta 219 (2016) 0–52, http://dx.doi.org/10.1016/j.electacta.2016.09.154.
[40] P. Pietsch, D. Westhoff, J. Feinauer, J. Eller, F. Marone, M. Stampanoni, V. Schmidt, V. Wood, silicon-graphite lithium ion battery anodes, Nat. Commun. 7 (2016) 1–11, http://dx.doi.org/10.1038/ncomms12909.
[41] D.C. Montgomery, G.C. Runger, Applied Statistic and Probability for Engineers, fifth ed., John Wiley & Sons, Inc, 2011.
[42] Y. Sun, N. Liu, Y. Cui, Promises and challenges of nanomaterials for lithium-based rechargeable batteries, Nat. Energy (June) (2016) 16071, http://dx.doi.org/10.1038/nenergy.2016.71.
[43] Volkswagen, 2016. Departure Time Programming, http://volkswagen-carnet.com/int/en/start/app-overview/e-remote/e%7b%5f}manager%7b%5f%7ddeparture.html%7b%23%7dtab/open/c63c6696-cd5e-4460-9de3-cf18673ac59f.
[44] M. Steinbuch, Tesla Model S Battery Degradation Data, 2015. https://steinbuch.wordpress.com/2015/01/24/tesla-model-s-battery-degradation-data/.
[45] C. Fleischer, W. Waag, H.-M. Heyn, D.U. Sauer, On-line adaptive battery impedance parameter and state estimation considering physical principles in reduced order equivalent circuit battery models part 2. Parameter and state estimation, J. Power Sources 262 (2014) 457–482, http://dx.doi.org/10.1016/j.jpowsour.2014.03.046.
[46] L. Lavigne, J. Sabatier, J.M. Francisco, F. Guillemard, A. Noury, Lithium-ion Open Circuit Voltage (OCV) curve modelling and its ageing adjustment, J. Power Sources 324 (2016) 694–703, http://dx.doi.org/10.1016/j.jpowsour.2016.05.121.
[47] A. Marongiu, N. Nlandi, Y. Rong, D.U. Sauer, On-board capacity estimation of lithium iron phosphate batteries by means of half-cell curves, J. Power Sources 324 (2016) 158–169, http://dx.doi.org/10.1016/j.jpowsour.2016.05.041.